Boletim da Sociedade Astronômica Brasileira, **35**, no. 1, 298-303

Calibration method for star cluster ages with *Gaia* DR2 data

Filipe A. Ferreira[1], J. F. C. Santos Jr.[1], & W. J. B. Corradi[1,2]

[1] DF-ICEx-UFMG e-mail: filipe1906@ufmg.br,jsantos@fisica.ufmg.br
[2] LNA e-mail: wbcorradi@gmail.com

Abstract. Star clusters are important objects for understanding how stars evolve. Their Color- Magnitude Diagrams (CMDs) show the effects of stellar evolution of coeval objects of same chemical composition. Furthermore, the determination of their astrophysical parameters (age, distance, colour excess and metallicity) together with their spatial distribution provides information about the structure and the evolution of the Galaxy itself. In this work, we used data from Gaia DR2 catalogs to produce a set of methodologies for characterization of open clusters, where precise memberlists, positions, mean astrometric parameters and radii were obtained. Using Gaia photometry, we carried out unprecedented age calibrations that rly on CMD morphological indices based on color ($\Delta(G_{BP} - G_{RP})_0$) and magnitude ($\Delta G$) differences between the red clump and the turnoff for a sample of 34 open clusters with ages covering the interval $8.3 < \log[t(\mathrm{yr})] < 9.9$. Our results show that PARSEC stellar evolution models tend to predict the difference ΔG. However, they fail to demonstrate the difference $\Delta(G_{BP} - G_{RP})_0$ for objects younger than $\log[t(\mathrm{yr})] = 8.8$, overestimating it.

Resumo. Aglomerados estelares são importantes objetos para o entendimento de como as estrelas evoluem. Seus Diagramas Cor-Magnitude (CMDs) refletem os efeitos da evolução estelar de objetos de mesma idade e composição química. Além disso a determinação de seus parâmetros astrofísicos (idade, distância, excesso de cor e metalicidade) juntamente com suas distribuições espaciais, fornece informações sobre a estrutura e a evolução da própria Galáxia. Neste trabalho, utilizamos dados dos catálogos Gaia DR2 para desenvolver um conjunto de metodologias para a caracterização de aglomerados abertos, que nos permitiram obter listas de membros precisas, coordenadas equatoriais, parâmetros astrométricos médios e raios. A partir da fotometria do Gaia, realizamos calibrações inéditas de idades usando índices morfológicos dos CMDs baseados nas diferenças de cor ($\Delta(G_{BP} - G_{RP})_0$) e magnitude ($\Delta G$) entre o clump de gigantes e o turnoff para um conjunto de 34 aglomerados abertos com idades compreendidas entre $8.3 < \log[t(\mathrm{yr})] < 9.9$. Como resultado, notamos que os modelos de evolução estelar PARSEC mostram bom acordo em reproduzir a diferença ΔG, porém falhando em demonstrar a diferença $\Delta(G_{BP} - G_{RP})_0$ para idades inferiores a $\log[t(\mathrm{yr})] = 8.8$, superestimando-a.

Keywords. (Galaxy:) open clusters and associations: general – Stars: evolution – (Stars:) Hertzsprung-Russell and C-M diagrams

1. Introduction

After the main sequence (ms) phase, the longest subsequent evolutionary stage in the life of a star is the Helium burning phase in the core. Observationally, in the HR diagram, this evolutionary phase is characterized by a concentration of cold and luminous stars, which feature is often referred as the Red Clump (RC). This feature is not often observed in young star clusters CMDs, as the Helium burning phase is rapid in more massive stars, which form less frequently. On the other hand, it is easy to notice the presence of a RC in observational HR diagrams of stellar populations and CMDs of evolved star clusters (Gaia Collaboration et al. 2018). The RC is widely used as a type of standard candle, because although the colors of stars in this evolutionary phase depend strongly on age and metallicity, for low-mass stars, the absolute magnitude tends not to show large variations, especially in the infrared. In this way, by establishing the reliable mean magnitude value of the RC for old populations, we are capable to determine distances to structures within our Galaxy and to neighboring galaxies (Grocholski & Sarajedini 2002, van Helshoecht & Groenewegen 2007, Bilir et al. 2013, Girardi 2016, Onozato et al. 2019.

The average position of the RC stars in the CMD can also be used as an age indicator. Indices based on CMD morphology are common in the literature, for example, the difference in magnitude between the main sequence turnoff (bluest point on the main sequence) and the mean magnitude of the RC is a well-known age indicator for Galactic clusters (Anthony-Twarog & Twarog 1985 , Phelps et al. 1994, Salaris et al. 2004, Piatti et al. 2010, Beletsky et al. 2009, Oralhan et al. 2015) and for Magellanic Clouds clusters (Geisler et al. 1997, Parisi et al. 2014). This age determination technique is independent of distance and reddening, but it is necessary the precise identification of those regions in the CMDs.

Phelps et al. (1994) defined the morphological age indices δV and $\delta 1$. The index δV is the difference between the inflection point of the main sequence or the base of the giant branch and the mean magnitude value of the RC, while $\delta 1$ is the colour difference between the point one magnitude brighter than the turnoff and the base of the giant branch. The index δV established in Phelps et al. (1994) was later calibrated with the ages and metallicities of star clusters in Salaris et al. (2004).

Widely used as an age indicator, the magnitude difference between the turnoff point (now as the bluest point on the main sequence) and the RC, both in visible light (ΔV, Carraro et al. (2004)) as well as infrared (ΔK, Beletsky et al. 2009, Zasowski et al. 2013), is a morphological age indicator that also is independent of colour excess and distance.

In this work, we use data from Gaia DR2 catalogs to establish morphological age indices for a set of Galactic open clusters from *Gaia* passbands, extending the morphological age indices for open clusters (OCs) as young as $\log[t(\mathrm{yr})] = 8.3$. We also present an age calibration with those indices.

This paper is structured as follows. In Section 2 the data is presented. In Section 3 the OC sample selection is described. In Section 4 the analysis procedures are developed, including membership assessment and determination of astrometric parameters. Morphological age indices are established in Section 5. The main results are presented in Section 6 and the concluding remarks are given in Section 7.

2. Data

The *Gaia DR2* catalogue provides positions, proper motions in right ascension and declination, parallaxes and photometry (G, G_{BP}, and G_{RP} passbands) for more than 1.3 billion sources (Evans et al. 2018; Gaia Collaboration et al. 2018a).

We have extracted Gaia DR2 data using the Vizier service. We used equations (1), (2), and (3) from Arenou et al. (2018) in order to clean our work sample from contamination due to double stars, astrometric effects from binary stars and calibration problems. This is a recommended basic filtering procedure aimed to assure the best quality of the data for analysis. We also adopted a filter by keeping stars with $G < 18$ to avoid less informative sources.

3. The OC sample

To select our OC sample, we used data from Netopil et al. 2016, which present a list of OCs with ages and metallicities based on [Fe/H] abundances. We restricted their sample to objects closer than 3 kpc from the Sun according to Dias et al. (2002) and for which metallicities were taken from high resolution spectroscopy. From the remaining sample, we kept OCs for which we could visually identify a concentration of stars around the RC position in the cluster CMD, resulting in a final sample of 34 OCs, covering $8.3 < log t[yr] < 9.9$ and $-0.44 < [Fe/H] < 0.37$.

4. Methodology

To assess stars memberships and remove the field population from the clusters populations, we employed proper motion and parallax selections of members. For this propose, we developed a methodology based on Ferreira et al. (2019) that includes the use of colour filters, the building of radial density profiles (RDPs) and the selection of members based on Gaussian fittings over the proper motion and parallax distributions.

4.1. The clusters proper motion detection

To find the OCs signatures in the Vector Point Diagram (VPD), we used the same method adopted in Ferreira et al. (2019), where a colour filter is applied on the sample to discard very reddened field stars and maximize the contrast between cluster and field population. Initially we started with a color threshold value $G_{BP} - G_{RP} < 2.5$ and, for the cases of more distant and severely contaminated clusters, we increased this threshold value, in order to make the initial detection of the cluster as an overdensity in the VPD. We then computed the peak values of the proper motions in right ascension and declination.

4.1.1. The proper motion filter

In order to estimate how the proper motion dispersions of real OCs behave (on average) as a function of distance, we separated a sample of 1229 OCs from Cantat-Gaudin et al. (2018) into intervals of 100 pc and calculated the mean dispersion values over each bin. We note that near clusters tend to exhibit higher dispersion values, due to the apparent random motion of the stars being greater. On the other hand, it is also possible to notice that clusters located at distances further than 1 kpc tend (on average) to exhibit an approximately fixed value, which shows that beyond this limit the physical dispersion of proper motions tends to be negligible in face of astrometric errors. In this way, we adopted an exponential fitting over these data to reproduce this behavior of the proper motion components (Fig. 1).

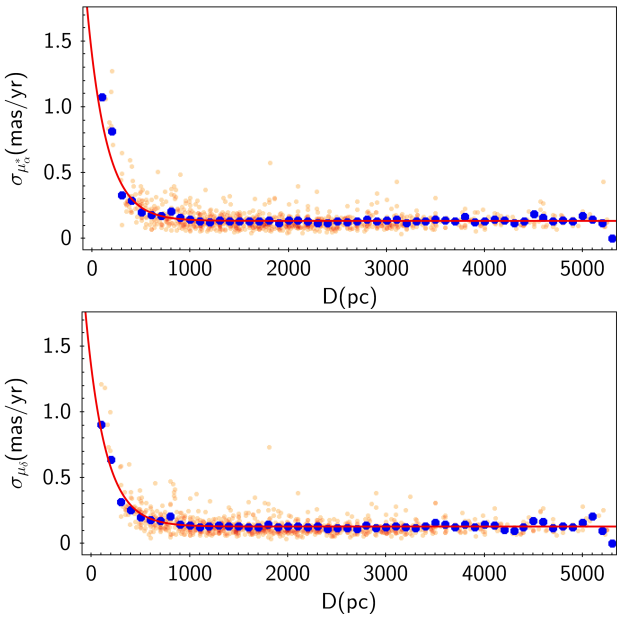

Figure 1. Mean values of μ_α^* (top) and μ_δ (bottom) dispersion for a set of 1229 OCs as a function of the heliocentric distance. The red lines represent the best exponential fitting, the red sample represent the density of OCs and blue filled circles the local mean value of proper motion dispersion.

This procedure was carried out to construct proper motion masks of sizes that fit clusters proper motion spaces of different distances. From the values of representative averages of dispersion, σ_{rep}, we adopted boxes with sides equal to 20 times this value, that is, we limited the samples of stars within $10\sigma_{rep}$ in around the peak values of proper motion components. In general, the sizes of the proper motion masks were:

$$L_{pmra} = 20 \times [1.229 \times exp(-0.005 \times D_{cluster}) + 0.136] \quad (1)$$

$$L_{pmde} = 20 \times [1.190 \times exp(-0.005 \times D_{cluster}) + 0.131] \quad (2)$$

Where $D_{cluster}$ is the distance according to Dias et al. (2002) and L_{pmra} and L_{pmde} the sizes of the mask in proper motion units in right ascension and declination, respectively. For subsequent analyses, we will abandon any color filters, as they obviously exclude very cool low main sequence stars from nearby clusters and possible red giant branch stars for some older clusters. We restricted the OCs proper motion space by employing the box-shaped filter centered on the calculated modal values of μ_α^* and μ_δ (Section 4.1.1) over the base sample in VPD space (left panel, Fig. 2). In the following procedures, we showed a set of examples of how our methodology performed on the open cluster NGC7789.

4.1.2. Centre and radial density profile

After establishing the size of the proper motion mask for our OCs sample, we applied it to the base samples to reduce the statistical influence of field stars, establishing subsamples. We constructed histograms with the equatorial coordinates of the stars and estimated the center values of the clusters in both coordinates through Gaussian fittings (taking the average values of the fitting).

We bult the RDPs the clusters by counting stars within concentric rings of the same thickness around the centre as a function of the distance from the ring to the centre. We repeated this

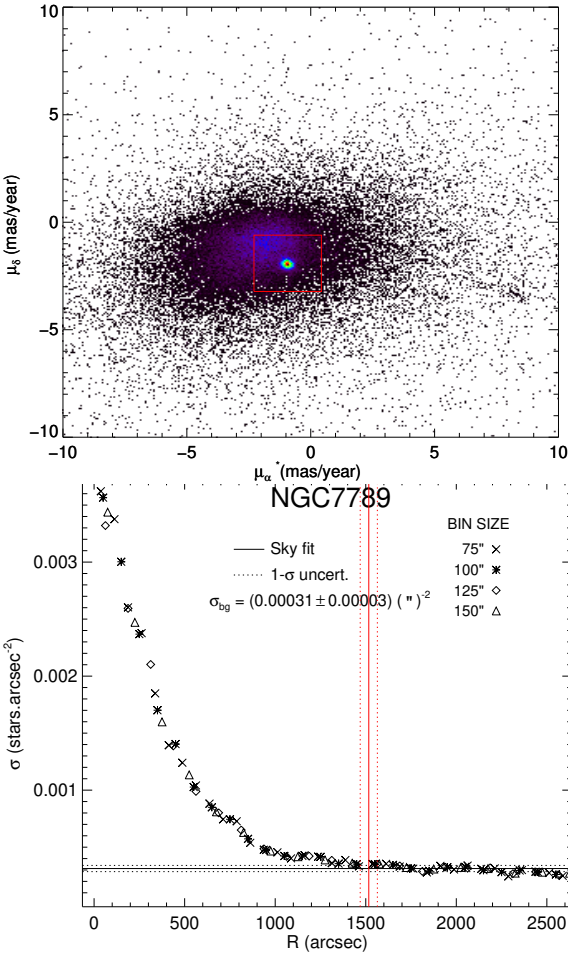

Figure 2. Top: Proper motion mask applied to the VPD from NGC 7789. Bottom: RDP constructed from the stellar density in the cluster region.

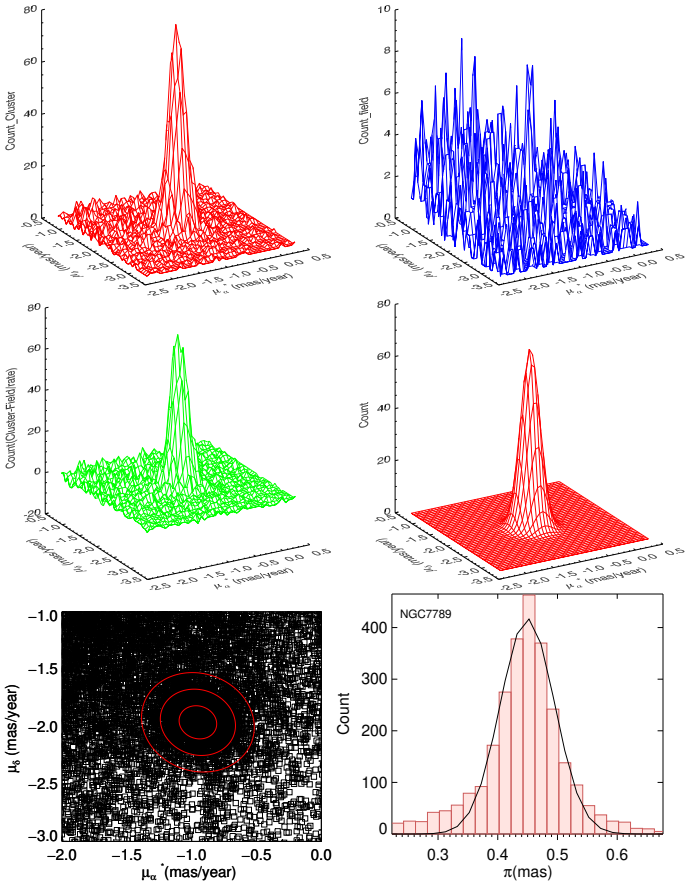

Figure 3. The proper motion membership procedure for NGC7789. Top left: two-dimensional histogram for the clusters VPD. Top right: the same, but for the control field. Middle left: Cluster-Field resulting histogram. Middle right: two-dimensional Gaussian fitting over the resulting histogram. Bottom left: Projection of the fitted function over the VPD, where the red ellipses represent the two-dimensional Gaussian dispersion in 1, 2 and 3-σ. Bottom right: one-dimensional Gaussian fitting over the parallax remaining sample.

procedure for 4 ring thicknesses (75, 100, 125 and 150 arcseconds) in order to mitigate binning effects on the density distribution. We also computed the density values of the sky far from the centre of the cluster. Then, we determined the value of the cluster's limiting radius as the distance at which the density level reaches the mean value computed for the sky background (right panel, Fig. 2). In this procedure, we applied small variations in the coordinates of the centre so that the density profile has a central maximum.

4.2. Two-dimensional proper motion filter and parallax filter

In order to obtain precise member lists, we established a filter capable of better predicting the morphology of the distribution of stars in the VPD, since the box-shaped masks tend to encompass regions substantially larger than the dispersions expected for the clusters.

For this propose, we constructed a two-dimensional histogram of the VPD with the samples restricted by the limit radius determined for the cluster. Then we also constructed two-dimensional histograms for an adjacent star field and with same area as the cluster: the internal radius of the control field is 1.3 times greater than the limiting radius and the external radius is established in such a way that the areas of the cluster and the field are equal. In order to remove the contribution of field stars in the proper motion space, we subtracted the histograms and performed 2D Gaussian fittings over the resulting histograms. This procedure is showed in Fig. 3. Then, proper motion outliers, i.e., those stars with proper motion components outside 3-σ of the 2D Gaussian mean values, were removed from the sample.

To discard remaining probable field stars with discrepant parallaxes from the average OC parallax, we performed an one-dimensional Gaussian fitting to the parallaxes of the sample filtered by proper motion, limiting them to 3-σ of the average value (Fig. 3).

4.3. Member lists

Our OCs member lists were obtained through the filters mentioned above. The panels in Fig. 4 show the members proper motions and parallaxes correlations, a cleaned CMD and the stars spatial distribution (sky chart).

5. CMDs: RC and turnoff positions

FWe determined the mean values and dispersion of colour ($G_{BP}-G_{RP}$) and magnitudes (G) of the RC by restricting the sample in a box with width of 1 mag for G and 0.4 mag for $G_{BP} - G_{RP}$, encompassing the region of concentration of RC stars. As uncer-

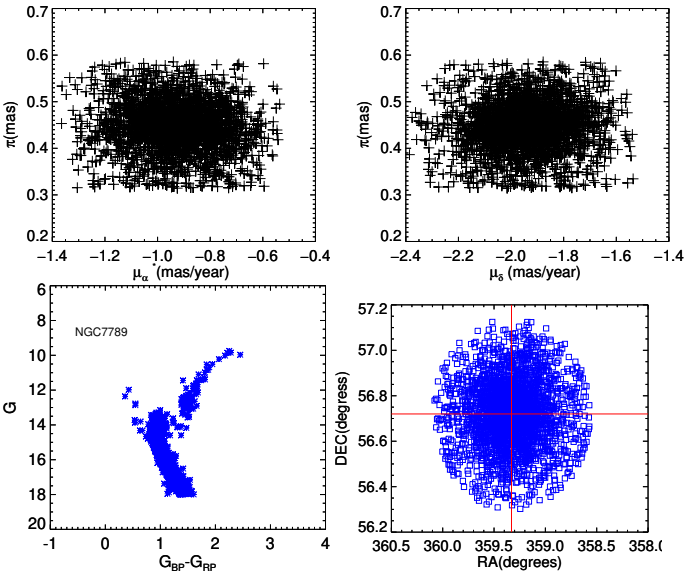

Figure 4. The final member list of NGC 7789 in different parameter spaces. Top left: Proper motions in right ascension vs parallax. Top right: Proper motions in declination vs parallax. Bottom left: A CMD with *Gaia* passsbands. A skychart, where the red cross represent the centre position.

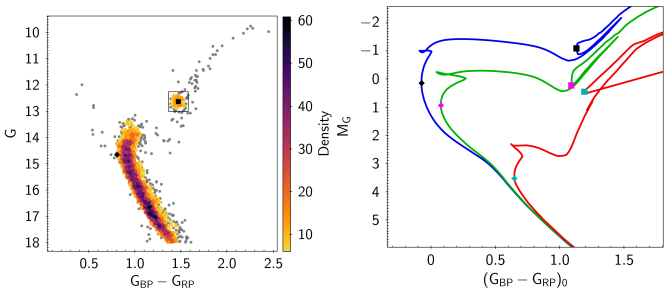

Figure 5. The figure represent the method used to calculate the colour and magnitude for RC and turnoff stars. Left: CMD of the OC NGC 7789 with the turnoff position (black diamond) and RC position (black square). The colour bar represent stellar density and the grey filled circles the removed stars. Right: The same calculus for solar metalicity PARSEC isochrones for the log[t(yr)] =8.4 (blue), 8.8 (green) and 9.5 (red).

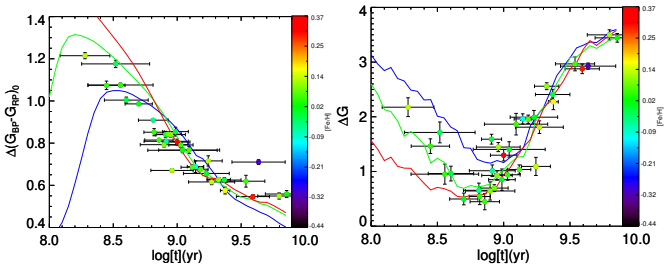

Figure 6. Left: Relation between $\Delta(G_{BP} - G_{RP})_0$ and log[t(yr)]. The colour bar represent the metalicity [Fe/H]. The lines represent the values from PARSEC isochrones, where the colours represent the maximum (red), minimum (blue) and solar (green) values of $[Fe/H]$. Right: The same, but for the ΔG versus log[t(yr)] relation.

tainty of the RC colour and magnitude, we adopted the standard error.

We considered the bluest point of the ms as the turnoff position. In order to remove isolated stars, we calculated the number of nearest neighbors of each star from the CMD within squared boxes of width 0.05 mag. We removed stars with few close neighbors and, from the remaining sample, measured the colour and magnitude values of the bluest star present in the ms. To provide uncertainties, we adopted the standard deviation value of colour and magnitude of the 5 bluest ms stars. See Fig 5.

We also applied a similar procedure for these same evolutionary regions in the PARSEC isochrones (Bressan et al. 2012), with ages and metallicities representative of our OC sample. Initially we selected stars where the isochrone table *label* identifier was equal to 1 (ms) and 4, 5 and 6 (He-burning stars). The turnoff position was taken as the bluest point of stars with label=1, but we rejected the blue hook-like structure, that represents stars at the end of the main sequence, in order to maintain consistency with what has been done for OCs. In order to demarcate the position of the RC, we took the point of maximum effective temperature for stars with *label* between 4 and 6 (right panel, Fig 5).

6. Results and discussion

6.1. Morphological age indices and evolution with age

In this section we will investigate how turnoff-RC differences relate to age and metallicity. Using the quantities calculated in Section 5, we determined the indices ΔG as the difference in magnitude between the RC and the turnoff, as well as the colour difference $\Delta(G_{BP} - G_{RP})_0$.

The panels in Figure 6 show how the indices ΔG and $\Delta(G_{BP} - G_{RP})_0$ behave with age and metallicity. It is evident that there appear to be two approximate linear relationships of ΔG with log[t]: one for objects with ages younger than $log[t(yr)] \sim 8.8$ and another for objects older than this limit. Metallicity does not appear to affect strongly the ΔG values for $log[t(yr)] > 9.0$, which has already been verified by other authors (Phelps et al 1994, Carraro et al. 2004, Salaris et al. 2004, Beletsky et al. 2009).

According to our data and the PARSEC models, the index $\Delta(G_{BP} - G_{RP})_0$ also shows little dependence on metallicity for objects older than $log[t(yr)] \sim 8.8$. The models show a more significant dependence on age and metallicity for younger objects. See Fig. 6.

The models show good agreement with the data on the relation ΔG versus $log[t(yr)]$. Regarding the values of $\Delta(G_{BP} - G_{RP})_0$, apparently for younger objects ($log[t(yr)] < 8.8$), the isochrones tend to overestimate this index, which is related to the prediction of redder RC in this regime of ages. The models also appear to fail to predict the values of $\Delta(G_{BP} - G_{RP})_0$ for objects older than $log[t(yr)] = 9.5$.

6.2. Age calibrations

An age calibration relationship for *Gaia* data (ΔG index) is not yet available in the literature, so here we will provide relations of calibration for the G band for the first time. For the OCs sample older than $log[t(yr)] = 8.8$, we determined three calibrations similar to those present in Beletsky et al. (2009) for the index ΔG: linear (Eq. 3), quadratic (Eq. 4) and a relation taking into account the metallicity (Eq. 5). See top panel of Fig. 7.

$$\log[t(yr)] = 8.67(\pm0.04) + 0.31(\pm0.02) \times \Delta G \quad (3)$$

$$\log[t(yr)] = 8.74(\pm0.08) + 0.22(\pm0.11) \times \Delta G + 0.02(\pm0.03) \times (\Delta G)^2 \quad (4)$$

$$\log[t(yr)] = 8.67(\pm0.04) + 0.30(\pm0.02) \times \Delta G - 0.02(\pm0.13) \times [Fe/H] \quad (5)$$

Table 1. Coefficients of the relationship established in Equation 6.

a	b	c	d	e	f
9.22 ± 0.33	−0.15 ± 0.07	0.09 ± 0.02	0.77 ± 1.46	−1.28 ± 0.80	−0.13 ± 0.13

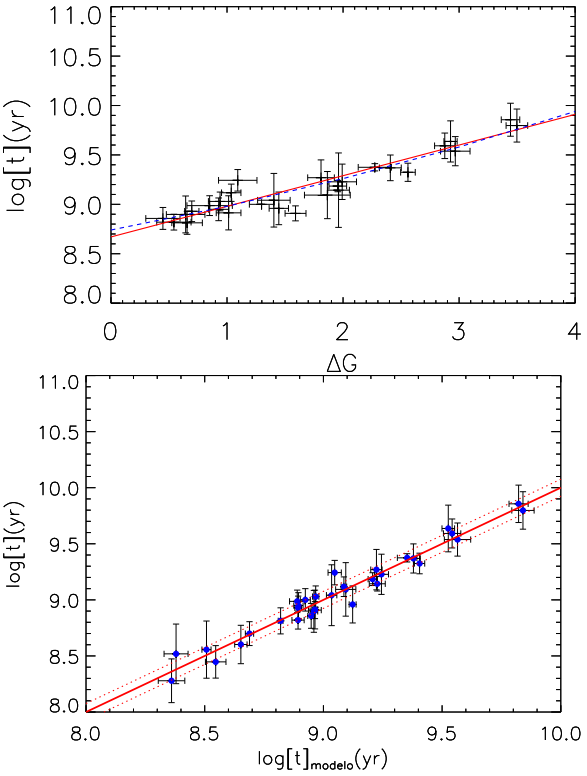

Figure 7. Top: Linear (red line) and quadratic (blue dotted line) of the relation ΔG versus log[t(yr)]. Bottom: General formula, where the x axis is represented by the model stabilised in Eq. 6.

As seen in the previous section and already evidenced by other authors (Phelps et al. 1994, Carraro et al. 1994, Salaris et al. 2004, Beletsky et al. 2009), the dependence of the index ΔG with metallicity is small, so that in many cases the metallicity term can be neglected. As a practical way of determine clusters ages, as accurate metallicity determinations are scarce in the literature, then equation 3 becomes a robust tool for determining ages of Galactic OCs.

6.3. General formula

As seen in the left panels of Figure 6, when we take into account the relation log[$t(yr)$] *versus* ΔG, we realize that objects with ages in the range $8.3 < \log[t(yr)] < 8.8$ may have the same ΔG values as those of $8.8 < \log[t(yr)] < 9.5$. However, the parameter $\Delta(G_{BP} - G_{BP})_0$ has an almost linear dependence on age, i.e., younger objects exhibit greater $\Delta(G_{BP} - G_{BP})_0$ than the older ones. In this case, using the index $\Delta(G_{BP} - G_{BP})_0$ breaks the ambiguity of the ΔG values of objects within the two mentioned age ranges. Thus, by extending the age calibration to ages $\sim 8.3 < \log[t(yr)] < 9.0$, we were able to establish a fitting function with quadratic and linear terms of both indices ΔG and $\Delta(G_{BP} - G_{BP})_0$ and a metallicity term (Eq.6 and Table 1). The fitting function is showed in Figure 7, where we note a small residual. This equation represent an important tool to determine ages for OCs with a wide range of ages.

$$\log[t(yr)] = a + b\Delta G + c\,(\Delta G)^2 + d\Delta(G_{BP}-G_{RP})_0 + e(\Delta(G_{BP}-G_{RP})_0)^2 + f[Fe/H] \quad (6)$$

7. Conclusions

In this work we were able to obtain accurate member lists for a set of 34 star clusters from accurate astrometry and photometry from *Gaia* DR2 data using an uniform methodology. CMDs were constructed and morphological age indices were measured.

Comparisons of the established indices showed that the models tend to satisfactorily predict the ΔG index for the entire age range here explored. But for ages $\log[t(yr)] < 8.8$, the models tend to present the index $\Delta(G_{BP} - G_{RP})_0$ systematically greater than observed (probably an effect of unresolved binary stars) and which can also be seen in several isochrone fittings in the literature (Piatti et al. 2011, Holanda et al. 2022, Martinez et al. 2020, Bossini et al. 2019). According to our data, the models also fail to predict the index $\Delta(G_{BP} - G_{RP})_0$ for older objects ($\log[t(yr)] > 9.6$), which indicates that for these two age ranges models do not match observations. This may be caused by a combination of effects such as unresolved binary stars, mass distribution of the giant progenitors of RC stars, differential reddening or the presence of secondary RC stars, making the average RC value bluer. Uncertainties of transformations from the theoretical to the observational plane also play a role.

Acknowledgements. The authors wish to thank the Brazilian financial agencies FAPEMIG, CNPq and CAPES (finance code 001). W. Corradi wishes to thank the LNA staff. This research has made use of the VizieR catalogue access tool, CDS, Strasbourg, France and has made use of data from the European Space Agency (ESA) mission *Gaia* (`https://www.cosmos.esa.int/gaia`), processed by the *Gaia* Data Processing and Analysis Consortium (DPAC, `https://www.cosmos.esa.int/web/gaia/dpac/consortium`). Funding for the DPAC has been provided by national institutions, in particular the institutions participating in the *Gaia* Multilateral Agreement.

References

Anthony-Twarog, B. J., & Twarog, B. A., 1985, ApJ, v. 291, p. 595, 1985
Arenou, F. et al., 2018, A&A, v. 616, p. A17, 2018.
Beletsky, Y.; Carraro, G.; Ivanov, V. D., 2009, A&A, v. 508, n. 3, p. 1279, 2009.
Bilir, S. et al. 2013, Ap&SS, v. 344, n. 2, p. 417, 2013.
Bossini, D. et al., 2019, A&A, v. 623, p. A108, 2019.
Bressan, A. et al., 2012, MNRAS, v. 427, p. 127, 2012.
Cantat-Gaudin, T. et al., 2018, A&A, v. 618, p. A93, 2018.
Carraro, G.; Chiosi, C., 2004, A&A, v. 287, p. 761, 1994.
Dias, W. S. et al., 2002, A&A, v. 389, p. 871, 2002.
Ferreira, F. A. et al., 2019, MNRAS, v. 483, p. 5508, 2019.
Gaia Collaboration et al., 2018 A&A, v. 616, p. A10, 2018.
Geisler, D. et al., 1997, AJ, v. 114, p. 1920, 1997.
Girardi, L., 2016, ARA&A, v. 54, p. 95, 2016.
Grocholski, A. J.; Sarajedini, A., 2002, AJ, v. 123, n. 3, p. 1603, 2002.
Holanda, N. et al., 2022, MNRAS, v. 516, n. 3, p. 4484, 2022.
Martinez, C. F. et al., 2020, MNRAS, v. 494, n. 1, p. 1470, 2020.
Netopil, M. et al., 2016, A&A, v. 585, p. A150, 2016.
Onozato, H. et al., 2019, MNRAS, v. 486, n. 4, p. 5600, 2019.
Oralhan, İ. A. et al., 2015, New A, v. 34, p. 195, 2015.
Parisi, M. C. et al., 2014, AJ, v. 147, n. 4, p. 71, 2014.
Phelps, R. L.; Janes, K. A.; Montgomery, K. A., 1994, AJ, v. 107, p. 1079, 1994.
Piatti, A. E. et al., 2011, MNRAS, v. 417, n. 2, p. 1559, 2011.
Piatti, A. E.; Clariá, J. J.; Ahumada, A. V., 2010, MNRAS, v. 402, n. 4, p. 2720, 2010
Salaris, M.; Weiss, A.; Percival, S. M., 2004, A&A, v. 414, p. 163, 2004.
van Helshoecht, V.; Groenewegen, M. A. T., 2007, A&A, v. 463, n. 2, p. 559, 2007.
Zasowski, G. et al., 2013, AJ, v. 146, n. 3, p. 64, 2013.